Zheng Xiaojiao (Orcid ID: 0000-0002-2863-0819)
McBeck Jessica (Orcid ID: 0000-0002-4465-5522)
Jamtveit Bjorn (Orcid ID: 0000-0001-5700-1803)
Zhu Wenlu (Orcid ID: 0000-0001-8166-7357)
Renard François (Orcid ID: 0000-0002-5125-5930)

# Mixed-mode strain localization generated by hydration reaction at crustal conditions

**Xiaojiao Zheng[1], Benoît Cordonnier[1, 2], Jessica McBeck[1], Elodie Boller[2], Bjørn Jamtveit[1], Wenlu Zhu[3], and François Renard[1, 4]**

[1]The Njord Centre, Physics of Geological Processes, Department of Geosciences, University of Oslo, box 1048, Blindern, 0316 Oslo, Norway.

[2]ESRF – The European Synchrotron, CS40220, Grenoble 38043, France.

[3] Department of Geology, University of Maryland, College Park, MD 20742, USA.

[4]University Grenoble Alpes, University Savoie Mont Blanc, CNRS, IRD, IFSTTAR, ISTerre, 38000 Grenoble, France.

Corresponding author: Xiaojiao Zheng (xiaojiao.zheng@geo.uio.no)

This article has been accepted for publication and undergone full peer review but has not been through the copyediting, typesetting, pagination and proofreading process which may lead to differences between this version and the Version of Record. Please cite this article as doi: 10.1029/2018JB017008

© 2019 American Geophysical Union. All rights reserved.

Accepted Article

Accepted Article

**Abstract**

Hydration reactions influence rock density and rheology. For example, volume increases produced in hydration reactions may generate sufficient tensile and shear stress to fracture both the rock undergoing the reaction and the surrounding host rock. We performed in situ dynamic X-ray synchrotron microtomography experiments to investigate reaction-induced fracturing. Two experiments on hydration of periclase were performed at 180 or 190°C, under a confinement of 10 or 80 MPa, a pore fluid pressure of 5 MPa or 75 MPa, and with or without differential stress, respectively. The sample assembly consists of a periclase cylinder inserted into a central hole within a serpentinite cylinder. The reaction from periclase to brucite results in a large volume increase (110%), pushing the periclase/brucite against the serpentinite and ultimately breaking it. Using time-resolved three-dimensional imaging, we quantify the spatial and temporal distribution of the reaction-induced fractures. We perform digital volume correlation (DVC) analysis to obtain the incremental strain tensors throughout the hydration and fracturing process. We use numerical models to assess the distribution of stress within the serpentinite. The DVC results show mixed-mode strain localization. The von Mises strain, indicative of shear, increases by a larger percentage than the contractive or dilatative strain components as the reaction-induced fractures grow. The distribution of von Mises strain follows a power law relationship in the cumulative frequency-magnitude domain, indicative of long-range elastic stress interactions during fracturing. This experimental finding sheds insights on the mechanisms of microseismicity measured in areas undergoing active serpentinization.

**Key Points:**

- Reaction-induced fracturing of periclase produces self-sustained hydration to brucite.
- The hydration reaction generates sufficient tensile stress to fracture a confining serpentinite cylinder.
- Strain localization in the serpentinite includes both tensile and shear components with a power law distribution of shear strain magnitudes.

© 2019 American Geophysical Union. All rights reserved.

Accepted Article

## 1 Introduction

Serpentinization of peridotite in the oceanic crust near low-velocity spreading ridges and subduction zones contribute to the Earth's water cycle, and influence the rheology of the oceanic and continental lithosphere (O'Hanley, 1992; Escartin et al., 1997; Malvoisin et al., 2012; Kelemen and Hirth, 2012; Hirth & Guillot, 2013; Guillot et al., 2015). Porosity, permeability, fluid flux and reactive surface area determine the extent of reaction because the limiting factor of the reaction is fluid supply (MacDonald and Fyfe, 1985; Jamtveit et al., 2008; Kelemen and Hirth, 2012).

Fully serpentinized peridotites are common worldwide, which suggests that fluid pathways remain open, or new pathways are continuously produced during reaction (MacDonald and Fyfe, 1985; Tutolo et al., 2016). Localized dissolution can contribute to porosity maintenance (Rouméjon et al., 2015; Lisabeth et al., 2017). However, the precipitation of serpentine minerals due to the transformation of peridotite, may also clog pores, reducing permeability and fluid flow (Andréani et al., 2009; Peuble et al., 2015). Serpentinization reaction produces a solid volume increase of 20-50%. The normal stresses produced in this expansion may fracture surrounding minerals (O'Hanley, 1996; Macdonald and Fyfe, 1985; Iyer et al, 2008; Kelemen and Hirth, 2012; Plümper et al., 2012). Such reaction-induced fractures will enhance the rate of hydration by generating new fluid pathways and reactive surface area, thereby providing a positive feedback (Rudge et al., 2010; Plümper et al., 2012; Xing et al., 2018). Field observations, numerical modelling, and *ex situ* and *in situ* experimental studies (Iyer et al., 2008; Ulven et al., 2014; Rouméjon et al., 2015; Malvoisin et al., 2017) have found evidence of reaction-induced fracturing during serpentinization. Reaction-induced fracturing is reported to occur in numerous other systems, such as carbonation of olivine (Kelemen and Matter, 2008; Kelemen and Hirth, 2012; Zhu et al., 2016; Van Noort et al., 2017; Lafay et al., 2018; Lambart et al., 2018), salt crystallization in cement or building stone (Scherer, 2004; Noiriel et al. 2010), and growth of travertine veins (Gratier et al., 2012).

Schlindwein and Schmid (2016) linked the unusually deep microseismicity observed at a slow-spreading ridge in the Indian Ocean to active serpentinization and fluid circulation at depth. More recently, Horning et al. (2018) showed that hydration reactions may generate micro-earthquakes in partly serpentinized peridotites at 3-7 km depths. However, the

© 2019 American Geophysical Union. All rights reserved.

underlying mechanics of serpentinization, and in general, hydration reaction induced seismicity, are not well understood. Microseismicity observed in the field usually have large shear components. However, the volume expansion during hydration reactions is generally thought to produce opening mode I cracks (e.g., Zhu et al., 2016).

To our knowledge, there is no systematic experimental investigation of the modes of strain localization during hydration reaction induced failure process. In the present study, we conducted two periclase hydration experiments at 180 or 190°C, under confinement of 10 or 80 MPa, pore fluid pressures of 5 MPa or 75 MPa, and with low or high axial stresses, respectively. Zheng et al (2018) showed that as long as the effective mean stress of the system is under 30 MPa, the periclase to brucite transformation will proceed to completion within a few hours and produces a volume increase of 110% (Kuleci et al., 2016). To study the modes of strain localization arising from reaction-induced fracturing, we inserted a periclase cylinder into a drilled hole within a serpentinite cylinder, and observed how the serpentinite deformed under the load produced by the transformation of periclase into brucite. The expanding periclase-brucite system exerted sufficient normal stresses on inside of the serpentinite to break it. In the present experimental study, we constrain the rate at which hydration reactions lead to fracturing of the host rock, as well as the evolving contributions of shear and tensile strain during fracturing. Our results provide new insights into the mechanics of microseismicity during active oceanic serpentinization.

## 2 Materials and Methods

### 2.1 Sample preparation

The serpentinite samples were taken from a block of carbonated serpentinite complex in Linnajavri, Norway (Beinlich et al., 2012). The serpentinite is composed of antigorite, minor dolomite, chromite, magnetite and accessory talc and tremolite. Two cylinders of 10 mm height and 5 mm diameter were cored. A hole of 5 mm depth and 2.3 or 2.7 mm diameter was drilled into the serpentinite cylinders (Fig. 1). Around the hole, the serpentinite wall thickness was in the range of 1.15 - 1.35 mm. Inside the hole, a cylinder with dimensions of 2.2 mm diameter and 5 mm height of periclase ceramic, similar to that used in Zheng et al. (2018), was inserted. The preparation technique necessitates a gap (<0.3 mm) between the periclase core and the serpentine wall, and the gap at the bottom of the hole (< 0.7 mm). The microstructure of the periclase and its composition measured by X-ray diffraction are shown in Figure S1. The periclase ceramic had an initial porosity between 0.8% and 1.5%, measured

© 2019 American Geophysical Union. All rights reserved.

at the resolution of the X-ray tomography images (Fig.1). Pores and several small preexisting cracks comprised the initial porosity. The reaction $MgO + H_2O \Leftrightarrow Mg(OH)_2$ has an associated solid volume increase of about 110% accompanying a 45% increase of solid mass during complete hydration with deionized water (Kuleci et al., 2016).

## 2.2 The HADES deformation apparatus

Each sample was placed in the triaxial deformation apparatus HADES (Renard et al., 2016), where the confining pressure, axial stress, pore fluid pressure and temperature can be controlled independently (Fig. 1). A jacket made of Viton fluoropolymer elastomer encased each sample, separating the confining medium (silicon oil) and the pore fluid (distilled water). HADES is almost transparent to X-rays and is mounted on a rotating stage at the X-ray tomography beamline ID19 at the European Synchrotron Radiation Facility (ESRF) in Grenoble, France. Schematic illustrations of the deformation apparatus and the experimental conditions are shown in Figure 1.

The radiographs were acquired with an exposure time of 6 ms, and 2500 projections were captured as the sample was rotated continuously over 180°. The total acquisition time was 180 seconds for each volume. Tomograms were acquired every 2-5 minutes during the progress of reaction. Two experiments under different stress conditions were conducted. Each run lasted for approximately 6 hours. The tomograms were then reconstructed with 16-bit gray level resolution and a voxel size of 6.5 micrometers, following the procedure of Zheng et al. (2018).

## 2.3 Experimental conditions

Two experiments, labelled Sp01 and Sp02, were performed at different confining pressures, $P_c$, pore pressures, $P_p$, and axial stresses, $\sigma_1$. The main parameter that we varied was the pore fluid pressure with experiment Sp01 performed under low pore pressure and experiment Sp02 performed under high pore pressure (Table1). A small fluid pressure gradient of 0.5 MPa was imposed between the pore fluid inlet and outlet of the sample to drive fluid flow. In the experiments, the confining pressure and axial load were imposed first, then the sample was heated at 2°C/minute until the desired temperature (180 or 190 °C), before the pore fluid pressure was increased to the desired value (Fig. 2). We did not observe damage created during the heating step. For experiment Sp01, we changed the loading conditions because the periclase had started to react and expand upward. We therefore increased the axial stress to enable fluid flow to the periclase/brucite. This loading change

© 2019 American Geophysical Union. All rights reserved.

produced the strain was detected by the digital volume correlation technique (see section §3.2). The reaction began when the axial stress was 50 MPa and the confining pressure was 10 MPa. This experiment was performed under a low fluid pressure of 5 MPa. Experiment Sp02 was performed at constant axial stress (81 MPa), confining pressure (80 MPa) and high fluid pressure (75 MPa). All the stresses indicated in Table 1 were imposed by the operators, and were not a result of the reaction. For both experiments we report the origin of time as when the pore fluid pressure was imposed, corresponding to the time when distilled water reached the sample.

### 2.4 Segmentation of tomograms

The 3D tomograms were post-processed with the software AvizoFire™. A workflow similar to that in Zheng et al. (2018) was applied. First, a nonlocal means filter was applied to reduce noise (Buades et al., 2005). The two solid parts in the sample, the serpentinite and the periclase, were masked and segmented separately (Fig. 3). In order to segment different phases at every time step, we calculated histograms of the gray value frequency distribution from 180 million voxels. Within the periclase cylinder, we measured changes in the volume fraction of periclase, brucite, and pore space. For the serpentinite volume, we segmented the fractures from the solid and calculated the change of the volume and spacing of these fractures as a function of time.

The porosity measured from CT data may be higher than that measured by helium or mercury porosimetry because mercury and helium could only reach connected pore throats (Njiekak et al., 2018). We measured the porosity through the built-in function of Avizo software (“connected component”) to acquire the connected porosity in our samples, following the procedure of Zheng et al. (2018). In this case the term “connected” stands for the automatically detected connected volumes, down to a minimum threshold size (set to 1 voxel). Pore voxels are interpreted to be connected in 3D if they share at least one common voxel-face.

### 2.5 Digital Volume Correlation analysis

Following the approach of McBeck et al. (2018) and Renard et al. (2018), we performed Digital Volume Correlation (DVC) analysis to obtain information on the evolution of the displacement field within the serpentinite (Fig. 4). Three-dimensional DVC analysis was first developed for engineering applications (Bay et al., 1999) and then applied to study of soils (Viggiani et al., 2004) and sandstones (Louis et al., 2007). We used the software

© 2019 American Geophysical Union. All rights reserved.

Tomowarp2 (Tudisco et al., 2017). DVC analysis searches for the displacements that maximize the correlation between voxel intensity subsets (sub-volumes) within pairs of sequential tomograms (Hall et al., 2010; Tudisco et al., 2015, 2017). By identifying similar patterns across successive volumes, DVC analysis produces 3D displacement fields from which the six independent components of the second rank 3D strain tensor may be calculated (Fig. 4). These incremental strain fields reveal strain localization that occurred within the time interval between the acquisitions of the pair of tomograms. The parameters used in DVC analyses may be tuned to capture contrasts in the X-ray attenuation coefficient fields, such as portions of grains, which can be recognized in successive tomogram pairs. Following systematic tests, we selected a correlation window size of 10 voxels (65 μm) and node spacing distance of 20 voxels (130 μm). The node spacing controls the spatial resolution of the calculated displacement fields, and consequently, the spatial resolution and magnitude of the components of the strain tensor. This choice ensured that each window contained a sub-volume with sufficient contrast to calculate a reliable correlation.

Following McBeck et al. (2018), we report changes in the local volumetric and shear strain fields using the first invariant of the incremental strain tensor, $I_1$, and the von Mises yield criterion equivalent strain, $(3J_2)^{1/2}$, where $J_2$ is the second invariant of the incremental strain deviator tensor, $J_2 = \frac{1}{3}{I_1}^2 - I_2$, and $I_1$ and $I_2$ are the first and second invariants of the incremental strain tensor. In the adopted sign convention, negative values of $I_1$ indicate net volumetric dilatancy, positive values of $I_1$ indicate net volumetric contraction, and $(3J_2)^{1/2}$ is used as a proxy for the magnitude of incremental shear strain. Following previous studies (McBeck et al., 2018, Renard et al., 2018), we kept only incremental strain values above the DVC resolution of $4\times10^{-3}$. Below this resolution, calculated DVC strain increments are within the noise of the DVC technique used here.

### 2.6 Mechanical modelling

To investigate the conditions required to produce tensile failure in the serpentinite, we build 2D linear elastic mechanical models of horizontal slices of the serpentinite portion of the experiment using the boundary element method code Fric2D (Cooke & Pollard, 1997). Fric2D solves the quasi-static equations of deformation to determine the displacements and stresses throughout a 2D plane strain model produced by a given set of boundary conditions (e.g., Cooke & Pollard, 1997). Boundaries are discretized into linear elements that may translate, rotate, open or slip in response to tractions or displacements applied to them.

© 2019 American Geophysical Union. All rights reserved.

Fric2D enables sampling the displacement and stress fields throughout the model produced by the loading conditions. Fric2D is available as part of the GROW package tools available on GitHub.

In the present study, we build models that represent a quarter section of a horizontal slice of the serpentinite cylinder. The radii of the inner and outer concentric circles that define the model boundaries matches those of the experiments. The inner circular model boundary represents the boundary between the serpentinite and periclase/brucite. The outer circular model boundary represents the boundary between the serpentinite and confining jacket. The planar model boundaries that connect the inner and outer boundaries are free to displace laterally (no shear tractions), and are fixed with no normal displacements. We set the confining stress on the outside of the serpentinite cylinder constant at 20 MPa. To constrain the normal stress required to break the serpentinite cylinder, we ran a series of models with different normal stresses exerted on the inner wall. The prescribed elastic modulus (50 GPa) and Poisson's ratio (0.25) are within the range of laboratory measurements of serpentinite (Song et al., 2004).

## 3 Results

### 3.1 Phase and microstructure evolution

In this study, the effective mean stress in experiments Sp01 and Sp02 was below 30 MPa (Table 1), and the reaction-induced fracturing was observed within the time scale of the experiments (Zheng et al., 2018). The early stages of the hydration process in the periclase core were consistent with the observations of Zheng et al. (2018). After an initially slow phase (stage 1), the replacement of periclase by brucite accelerated, and the periclase core started to fracture (Fig. 5). In our previous experiments on the transformation of periclase to brucite, the porosity initially increased, but subsequently decreased, generating a "porosity pulse" (Zheng et al., 2018). In the present experiments, however, the porosity (and replacement rate) generation reached a plateau (stage 2) followed by fracturing of the surrounding serpentinite cylinder (Fig. 5). After the fracturing of the serpentinite wall, the porosity in the periclase core of experiment Sp01 decreased slightly (stage 3). In experiment Sp02, the porosity continued to increase following fracturing and then stabilized.

In experiment Sp01 (Fig. 5a, Video S1), segmentation revealed evidence of brucite after 100 minutes. At 170 minutes, the porosity reached a plateau level of about 4.5%. After 220 minutes, the reaction was about 40% complete in terms of periclase consumption (Fig.

© 2019 American Geophysical Union. All rights reserved.

S2). The fracturing of the serpentinite wall began at 190 minutes, producing a slight increase and then decrease in the porosity of the periclase-brucite mixture. For experiment Sp02 (Fig. 5b, S2b, Video S2), brucite was observed after 150 minutes and fracturing of serpentinite started after 196 minutes. At 200 minutes, the periclase-brucite core reached a maximum porosity of 2.3%. After 340 minutes, the reaction was about 50% complete (Fig. S2).

During the experiments, the periclase grains fragmented, resulting in a decrease in grain size and an increase in number of distinct grains (Fig. 6a, b). At the initiation of the hydration process, there was only one periclase grain with a mean grain size of 5-7x$10^{-10}$ $m^3$. As the reaction progressed, the periclase volume gradually fragmented into smaller grains. At the end of the experiments, several large grains remained because the reactions were only ~40-50% complete.

3.2 Fracture development in the serpentinite

The volume expansion associated with the hydration of periclase led to fracturing of the surrounding serpentinite. Fracturing began when the imposed loading conditions were constant, and not during changes in differential stress. We analyzed the evolution of this fracture network as a function of time. The expanding periclase cylinder touched the inner wall of the serpentinite at around 160 minutes. The first cracks initiated from inner wall of the serpentinite cylinder in both Sp01 and Sp02 at 190 minutes and 196 minutes, respectively (Figs. 5c, 5d). The yellow arrows in Figure 5 indicates the moment when we observed the first fractures in each experiment at the voxel resolution of 6.5 micrometers of the tomograms. However, these fractures likely nucleated with apertures smaller than the 6.5 micrometers resolution, and so they likely nucleated earlier. These fractures grew and coalesced, forming a connected network (Fig. 7a, 8a). Most of the fractures opened perpendicular to the core boundary and extended from the periclase/brucite core to the outer wall of the serpentinite (Figs 5c, 5d, 7a, 8a). The first fractures nucleated at the inner wall of the serpentinite cylinder (Movies S5, S6). Then, before 200 minutes, the fracture apertures were wider near the outer serpentinite perimeter, and narrower toward the center because of the circular geometry of the serpentinite cylinder. Then, after 200 minutes, newly propagating fractures had wider apertures toward the center, except for the existing fractures that continued to widen. After 210 minutes, the fractures widened and gradually coalesced, forming a 3D network (Movies S7). Incremental strains calculated through DVC analysis (Figs. 7b-c, 8b-c) show that fracture development in the serpentinite produced mixed-mode strain localization, with dominantly shear and dilatant components.

© 2019 American Geophysical Union. All rights reserved.

Accepted Article

We calculated the incremental strain components using DVC analysis in both experiments. The incremental dilatant, contraction and shear strain both increased and decreased during the hydration induced deformation (Fig. 9a, b). The increase of normalized incremental strain values from 170-190 minutes in experiment Sp01 corresponds to a change in loading conditions. The significant increase of incremental contraction, dilatant and shear strain beginning at 195 minutes coincides with the first observations of fractures in experiment Sp01. These fractures formed shortly after the loading conditions changed, and the stress on the sample was constant. They were related to the force of crystallization exerted by the transforming periclase core. At around 210 minutes, the normalized strain components dropped and then became stable as preexisting fracture widened, and few or no new fractures nucleated. As the incremental strain magnitudes decreased, the rate of fracture spacing decreased (Fig. 10). For experiment Sp02, the incremental dilatant, contraction and shear strain also increased after the first observable fracture nucleated. Stabilization of the strain values occurred over a longer time period in experiment Sp02 than Sp01, probably because of the higher fluid pressure in Sp02. The sudden increase around 250 minutes can be related to the formation of a shear fracture larger than the other fractures (Movie S4). Here, the von Mises strain and dilatant components change more than the contraction component.

We analyzed the correlations in strain increment distributions by plotting the distribution of the shear strain increments above a value of $4 \times 10^{-3}$, which corresponds to the resolution of the DVC analyses used here. In a log-log representation, the shear strain increments show a straight-line distribution (Fig 9c), indicating power-law scaling over one order of magnitude in incremental shear strains. The slopes of the curves in Fig. 9 correspond to the exponent of these power laws and were calculated using a goodness-for-fit method (Clauset et al., 2009). The power law exponent was equal to $3.0 \pm 0.2$ for both experiments. This high value of the exponent indicates that the proportion of small shear strain increments is larger than large ones. This power law also indicates that long-range correlations developed in the volume during fracturing.

To characterize the topology of the fracture network within the serpentinite, we measured the spacing between fractures, and report the fracture spacing index, $N = H/S$, where $H$ is the thickness of the serpentinite layer and $S$ is the mean spacing between successive fractures (Price 2016), as shown in the sketch of Figure 10. The value of the thickness-spacing index depends on rock type (Harris et al., 1960; Narr, 1991). We calculated the spacing index in seven representative horizontal cross sections located at different vertical

© 2019 American Geophysical Union. All rights reserved.

positions above the solid base of the serpentinite cylinder at nine time steps (Fig. S2). For both experiments, the value of *N* increased during initiation of cracks in the serpentinite and stabilized at 50 minutes after the first fracture nucleated to values between 1 and 2 at the end of the experiment. For experiment Sp01, the *N* ratio was slightly smaller because fewer fractures were generated after the initial fracturing event.

3.3 Stress distribution in the serpentinite

In series of 2D linear elastic boundary element method models, increasing normal force exerted on the inner serpentinite wall captures the force of crystallization exerted (Fig. 11). This suite of models provides two critical predictions that are consistent with our new and previous experiments (Zheng et al., 2018). When the normal stress exerted on the inner wall reaches a threshold value, $\sigma_i$ >30 MPa, the normal stress within the serpentinite, $\sigma_{\theta\theta}$, becomes tensile, consistent with Lamé's solution (Jaeger and Cook, 1979). When $\sigma_i$ is between 30 and 35 MPa, the magnitude of $\sigma_{\theta\theta}$ exceeds the tensile strength of serpentinite (10 MPa, e.g., Ague et al., 1998). Zheng et al. (2018) observed that reaction-induced fracturing produced a crystallization pressure of at least 30 MPa. This limit of 30 MPa could arise in part from the visco-plastic strength of the porous material. If the material begins to compact and creep, the rate of reaction-induced fracturing may decrease (Skarbek et al., 2018). Our numerical models provide evidence that this value of the force of crystallization at the edge of the periclase/brucite core is sufficient to break the serpentinite.

The second critical prediction of these numerical models is that the highest tensile stresses will develop on the inner wall of the serpentinite (Fig. 11e, f). Examination of the tomograms indicates that the first observable fractures nucleated near the periclase/brucite-serpentinite interface, consistent with the higher tensile stresses produced in these regions in the models.

**4 Discussion**

3.1 Patterns of reaction-induced fracturing

In natural serpentinization, preexisting fracture networks provide fluid conduits for hydrating oceanic and upper mantle rocks. Olivine reacts with water to form serpentine, with a volume increase of 40-50%. The hydration reaction of periclase to brucite investigated here is analogous to natural serpentinization. The microstructure in the periclase core during its transformation into brucite (Fig. 12a) shows hierarchical patterns similar to the mesh structure of natural serpentinites (Fig. 12b). The fracture patterns in the serpentinite samples

© 2019 American Geophysical Union. All rights reserved.

in our experiments also appear similar to the patterns of veins and fracture networks observed in natural serpentinites (Fig. 12 c-d; see also Figure 5b in Andréani et al., 2007; Figure 4 in Rouméjon and Cannat, 2014; and Figure 5 in Kelemen et al., 2018).

In our experiments, reaction induced fractures in the serpentine samples were initiated perpendicular to the interface between the periclase core and the serpentine, forming a radial pattern (Figs. 10, 11a). Secondary fractures grow from these initial ones (Figs. 7a, 8a). Such patterns have been described as resulting from a hierarchical fracturing process (Iyer et al., 2008; Jamtveit et al., 2009; Plümper et al., 2012). Existing fractures may exhibit dilatancy hardening behavior due to suction that increases the effective normal stress on the crack surfaces, and promote the nucleation of new fractures (Rice, 1975; Ougier-Simonin and Zhu, 2013).

Meanwhile, an increase in pore pressure increase tends to promote the tensile failure of a low porosity rock shaped as a hollow cylinder (Hubbert and Wills, 1957; Schmitt and Zoback, 1992). The higher fracturing rate at the initiation of the experiments could arise in part from the higher rate of pore pressure increase (Figure 10).

At the last stage of our experiment, the hydration reached ~50% completion (Fig. 5). This degree of completion is consistent with observations of natural serpentinites collected in the Mid-Atlantic oceanic ridge, assuming that serpentinization occurred in a system conserving the mass of the initial minerals and open to fluids (Andréani et al., 2007). When the hydration degree is lower than 5%, the fractures at the origin of veins are generally tensile cracks that formed between 4 and 8 km depth in the mantle rock below the oceanic ridge (Andréani et al., 2007) or up to 30 km within the oceanic crust (Schlindwein and Schmid, 2016). Andréani et al. (2007) suggest that serpentinization stopped at 50% because in a closed system the fluid pressure decreases as the fluid is consumed in the reaction. Complete serpentinization would therefore require that the system evolves from a closed stated to an open state. Fracture propagation would allow further fluid infiltration. The generation of new fractures in the periclase core slowed when the reaction degree was 20% (Fig. 5). Rouméjon and Cannat (2014) observed that the reaction-induced fracturing process mainly occurred between 0-20% serpentinization in the Mid-Atlantic and Southwest Indian oceanic ridges. The plastic deformation of the weaker serpentine may enhance strain partitioning between the serpentine veins and olivine. Consequently, the rate of fracturing of the olivine may be reduced after 20% serpentinization.

© 2019 American Geophysical Union. All rights reserved.

Accepted Article

In experiment Sp01, the surface area of fractures was $0.8 \times 10^{-3}$ $m^2$ at the end of the experiment. The volume of the serpentinite hosting the fractures was $1.1 \times 10^{-7}$ $m^3$. Consequently, the reaction produced $7 \times 10^3$ $m^2$ of fracture surface area per cubic meter of partially serpentinized rock. In experiment Sp02, the reaction produced $5.5 \times 10^3$ $m^2$ of fracture surface area per cubic meter of partially serpentinized rock. These fractures create new reactive surfaces, increase the permeability and allow fluid access, sustaining the hydration of peridotite.

The surface energy necessary to create these fractures is of the order of 6±1 kJ/$m^3$ of rock, assuming a surface energy of 1 J/$m^2$, an upper bound for minerals. Zheng et al. (2018) estimated that the Gibbs free energy for the periclase-brucite transformation could be as high as 25 kJ/mol of periclase, corresponding to $2.2 \cdot 10^9$ J/$m^3$ of periclase when considering the molar volume of periclase of $11.248 \cdot 10^{-6}$ $m^3$/mol. This result suggests that the amount of strain energy converted to fracture energy in the serpentinite is negligible. Most of the thermodynamic energy was used as work against the confining pressure and heat dissipation during the experiments.

### 3.2 Effect of fluid pressure on the rate of serpentinite fracturing

In our experiments, the hydration reaction from periclase to brucite broke the surrounding serpentinite. This reaction and subsequent fracturing produced a positive feedback loop between the hydration reaction and fracturing. The expansion of the periclase/brucite composite against the surrounding serpentinite exerted sufficient normal stress in the tangential direction to nucleate fractures at the inner wall of the serpentinite. These fractures then propagated radially outward, and accommodated dilation and shear strain. As the fractures developed and accommodated strain, they increased the bulk porosity of the serpentinite, thereby increasing the reaction rate by channeling fresh fluid to unreacted surfaces.

The fracture spacing evolution of the two experiments follow similar trends: first high rates of decrease and then plateauing between 1 and 2 ratio of fracture spacing to layer thickness. However, the stabilization of the strain values occurred over a longer time period in experiment Sp02 (150 minutes) than Sp01 (15 minutes). The spatial distributions of the high incremental shear and dilative strains (Movies S3-S4) indicate that the propagation of new fractures coincided with increases in the incremental strain magnitudes, and that the continued opening of these fractures led to slower rates of strain accumulation (Figure 9). The higher pore pressure of experiment Sp02 (75 MPa) compared to experiment Sp01 (5

© 2019 American Geophysical Union. All rights reserved.

MPa) may have led to the longer period of strain rate increase and decrease in experiment Sp02 compared to experiment Sp01. Increasing pore pressure can reduce the brittle strength and influence slip instability (Ougier-Simonin and Zhu, 2013, 2015). At the same effective pressure, fracture propagation in antigorite serpentine samples is considerably slower at high pore fluid pressures (French and Zhu, 2017), similar to what is observed in our experiments.

### 3.3 Implications of reaction-induced fracture development

Serpentinization may induce strain localization and intermediate-depth seismicity (Raleigh and Paterson, 1965; Hacker et al. 2003). Schlindwein and Schmid (2016) proposed that the microseismicity observed in the South-West Indian mid-oceanic slow spreading ridge was related to active serpentinization, and that reaction-induced fractures could produce shear failure up to depths of 20 km. Consistent with these observations, our digital volume correlation analyses reveal concentrations of Von Mises incremental strain values, indicative of shear strain. The serpentinite samples may have failed initially as mode I cracks hosting tension. However, these fractures then hosted localized concentrations of shear strain, indicating that stress redistribution during reaction-induced fracturing can induce slip along pre-existing defects. This observation supports interpretations that microseismicity measured at slow-spreading ridges may arise from active serpentinization of the oceanic crust (Horning et al., 2018). This observation also underscores the prevalence of mixed-mode deformation, and the often false dichotomy of shear and tensile failure and deformation.

Earthquakes are not uniformly distributed in magnitude. Instead, the distribution of earthquake magnitude obeys a power-law, known as the Gutenberg-Richter magnitude-frequency relation. For worldwide seismicity, the power-law exponent *b*-value is close to 1.0. However, higher *b*-values have been observed in geothermal systems with local injections of fluids under high confining pressure (Bachmann et al., 2012). The *b*-values along convergent plate margins undergoing fluid production by dehydration reactions show also higher *b*-values in the range of 1.3 to 1.6 (Singh and Singh, 2015; Wiemer and Benoit, 1996).

We compare the statistics of strain distribution calculated using DVC in our experiments with the statistics of earthquake magnitudes observed in the crust. The Gutenberg-Richter magnitude-frequency relation can be expressed in seismic moment $M_0$, where the log-log plot of the cumulated number of earthquakes versus seismic moment is a straight line with a negative slope $\beta$~2/3$b$ (eqs. 6.6 and 7.2b in Ben-Zion, 2003). The seismic moment is defined by $M_0=GAd$, where $G$ is the shear modulus of the rock, $A$ is the rupture

© 2019 American Geophysical Union. All rights reserved.

area and $d$ is the slip distance. In our DVC calculation, the surface area, A, is proportional to the square of the correlation window size, $L$ if one considers that the shear strain is due to the slip of a small fault that cuts the entire correlation window. The shear strain, $\varepsilon_{vM}$, we calculate is related to a slip distance, $d$, and the size of the correlation window, $L$, such that $\varepsilon_{vM} = d/L$. As a consequence, the relationship between the von Mises strain, $\varepsilon_{vM}$, and the seismic moment can be approximated $M_0 = GL^3 \varepsilon_{vM}$, and the shear strain we measured using DVC is therefore proportional to $M_0$. We found that the magnitude distribution of the shear strain in the experiments follows a power law relationship (Fig. 9c) with a slope $\alpha$=-3.0 in a log-log plot of the frequency-moment distribution (eq. 7.1a in Ben-Zion, 2003), corresponding to a slope $\alpha+1=-2.0$ for a cumulated distribution (eq. 7.1b in Ben-Zion, 2003). Making an analogy with the Gutenberg-Richter law, our experimental law shows a power law exponent $\alpha+1=2/3b$. This power law exponent corresponds to a value of $b$=3.0 and $\beta$=2.0. We interpret this power law relationship as a manifestation of the elastic stress interactions in the serpentinite during deformation. Long-range elastic interactions play a key role during the failure of heterogeneous materials because heterogeneities may concentrate stress and reduce the overall material strength (e.g., Vasseur et al., 2015). The presence of heterogeneities may also change the relative size distribution of seismic events, represented by the $b$-value, to a larger proportion of small earthquakes (Scholz, 1968). The range of the strain data is limited at just over one order of magnitude. At the lower range, our strain data are limited by the imaging resolution; and at the higher range, the data are limited by the parameters of the DVC calculation, including the correlation window size and node size. While $\beta$~2/3 for earthquakes, the exponent of the power law of the shear strain magnitude distributions throughout each experiment is $\beta$~2.0. Whereas the $\beta$-value represents only the radiated seismic energy for earthquakes, the exponent of the strain magnitude distribution in our experiments represents the total shear strain energy. One plausible explanation of the larger exponent of strain magnitude distribution in our experiments (i.e., $\beta$=2.0) could be that strain events are aseismic.

**5 Conclusions**

The hydration of periclase into brucite generated enough stress to break the confining serpentinite cylinder. Our numerical modeling results indicate that the effective force of crystallization reached a magnitude of at least 30 MPa, consistent with previous experimental results (Zheng et al., 2018). The rate of fracture development at 5 MPa pore fluid pressure

© 2019 American Geophysical Union. All rights reserved.

and 45 MPa differential stress was higher than that at 75 MPa fluid pressure and 1 MPa differential stress, implying that fracture growth is sensitive to hydro-mechanical feedbacks. The fractures nucleated by the hydration reaction are mixed-mode, including both tensile and shear components. The magnitude distribution of the shear strain (i.e., von Mises strain) follows a power-law relationship over one order of strain magnitude, indicating the existence of long-range elastic interactions. These results provide experimental support that microseismicity may result from the serpentinization of deep oceanic crust at slow-spreading ridges.

**Acknowledgments**

The deformation apparatus was built by Sanchez Technology. This study received funding from the Norwegian Research Council (project HADES, grant 250661 to FR), the European Union (H2020 ERC Advanced Grant Agreement n°669972, 'Disequilibrium Metamorphism' to BJ). Beamtime was allocated at the European Synchrotron Radiation Facility (Long Term Proposal ES-295) and we thank Alexander Rack and Paul Tafforeau for the technical support. Data storage was provided by UNINETT Sigma2 - the National Infrastructure for High Performance Computing and Data Storage in Norway (project NS9073K). WZ was partially supported by the US National Science Foundation through EAR-1761912. The authors thank Dr. Oliver Plümper for providing image 12b, Dr. Stéphane Guillot for providing image 12 and Claire Aupart for helpful suggestions. We thank Douglas Schmitt, Holger Stunitz and Peter Kelemen who provided constructive reviews that helped improving the article.The X-ray tomography data (series of 3-D volumes, 16-bytes gray scale) supporting the conclusions are available on the National Norwegian data repository center: https://doi.org/10.11582/2018.00037. The boundary element numerical code Fric2D is available as part of the GROW package tools on GitHub (https://github.com/mlcooke/GROW).

**References**

Ague, J., Park, J., & Rye, D. (1998). Regional metamorphic dehydration and seismic hazard. *Geophysical research letters, 25*(22), 4221-4224.

Andréani, M., Mével, C., Boullier, A. M., & Escartin, J. (2007). Dynamic control on serpentine crystallization in veins: Constraints on hydration processes in oceanic peridotites. *Geochemistry, Geophysics, Geosystems*, 8(2).

Andreani, M., Luquot, L., Gouze, P., Godard, M., Hoise, E., & Gibert, B. (2009). Experimental study of carbon sequestration reactions controlled by the percolation of CO2-rich brine through peridotites. *Environmental Science & Technology, 43*(4), 1226-1231.

Bachmann, C.E., Wiemer, S., Goertz-Allmann, B., Woessner, J. (2012). Influence of pore-pressure on the event-size distribution of induced earthquakes. *Geophys. Res. Lett*. 39, L09302. http://dx.doi.org/10.1029/2012GL051480.

Bay, B. K., Smith, T. S., Fyhrie, D. P., & Saad, M. (1999). Digital volume correlation: three-dimensional strain mapping using X-ray tomography. *Experimental mechanics, 39*(3), 217-226.

Beinlich, A., Plümper, O., Hövelmann, J., Austrheim, H., & Jamtveit, B. (2012). Massive serpentinite carbonation at Linnajavri, N–Norway. *Terra Nova, 24*(6), 446-455.

© 2019 American Geophysical Union. All rights reserved.

Ben-Zion, Y., Lee, W. H. K., Kanamori, H., Jennings, P. C., & Kisslinger, C. (2003). Key formulas in earthquake seismology. *International handbook of earthquake and engineering seismology*, 81.

Buades, A., Coll, B., & Morel, J.-M. (2005). *A non-local algorithm for image denoising.* Paper presented at the Computer Society Conference on Computer Vision and Pattern Recognition, 2005. IEEE.

Clauset, A., Shalizi, C. R., & Newman, M. E. (2009). Power-law distributions in empirical data. *SIAM review*, 51(4), 661-703.

Cooke, M., & Pollard, D. (1997). Bedding-plane slip in initial stages of fault-related folding. *Journal of Structural Geology, 19*(3-4), 567-581.

Escartin, J., Hirth, G., & Evans, B. (1997). Effects of serpentinization on the lithospheric strength and the style of normal faulting at slow-spreading ridges. *Earth and Planetary Science Letters, 151*(3-4), 181-189.

French, M. E., & Zhu, W. (2017). Slow fault propagation in serpentinite under conditions of high pore fluid pressure. *Earth and Planetary Science Letters, 473*, 131-140.

Goff, F., & Lackner, K. (1998). Carbon dioxide sequestering using ultramafic rocks. *Environmental Geosciences, 5*(3), 89-101.

Gratier, J.-P., Frery, E., Deschamps, P., Røyne, A., Renard, F., Dysthe, D., Hamelin, B. (2012). How travertine veins grow from top to bottom and lift the rocks above them: The effect of crystallization force. *Geology, 40*(11), 1015-1018.

Guillot, S., Schwartz, S., Reynard, B., Agard, P., & Prigent, C. (2015). Tectonic significance of serpentinites. *Tectonophysics,* 646, 1-19.

Hall, S. A., Bornert, M., Desrues, J., Pannier, Y., Lenoir, N., Viggiani, G., & Bésuelle, P. (2010). Discrete and continuum analysis of localised deformation in sand using X-ray [mu] CT and volumetric digital image correlation. *Géotechnique, 60*(5), 315-322.

Hacker, B. R., Abers, G. A., & Peacock, S. M. (2003). Subduction factory 1. Theoretical mineralogy, densities, seismic wave speeds, and H2O contents. *Journal of Geophysical Research: Solid Earth, 108*(B1), https://doi.org/10.1029/2001JB001127.

Harris, J. F., Taylor, G. L., & Walper, J. L. (1960). Relation of deformational fractures in sedimentary rocks to regional and local structure. *AAPG Bulletin, 44*(12), 1853-1873.

Hirth, G., & Guillot, S. (2013). Rheology and tectonic significance of serpentinite. *Elements, 9*(2), 107-113.

Hubbert, M. K., & Willis, D. G. (1957). Mechanics of hydraulic fracturing. *Transactions of the American Institute of Mining and Metallurgical Engineers.* 210, 153-168.

Horning, G., Sohn, R. A., Canales, J. P., & Dunn, R. A. (2018). Local Seismicity of the Rainbow Massif on the Mid-Atlantic Ridge. *Journal of Geophysical Research: Solid Earth, 123*(2), 1615-1630.

Iyer, K., Jamtveit, B., Mathiesen, J., Malthe-Sørenssen, A., & Feder, J. (2008). Reaction-assisted hierarchical fracturing during serpentinization. *Earth and Planetary Science Letters, 267*(3-4), 503-516.

Jaeger, J. C., Cook, N. G., & Zimmerman, R. (2009). Fundamentals of rock mechanics. John Wiley & Sons.

Jamtveit, B., Malthe-Sørenssen, A., & Kostenko, O. (2008). Reaction enhanced permeability during retrogressive metamorphism. *Earth and Planetary Science Letters, 267*(3-4), 620-627.

Jamtveit, B., Putnis, C. V., & Malthe-Sørenssen, A. (2009). Reaction induced fracturing during replacement processes. *Contributions to Mineralogy and Petrology, 157*(1), 127-133.

Accepted Article

© 2019 American Geophysical Union. All rights reserved.

Kelemen, P. B., Aines, R., Bennett, E., Benson, S. M., Carter, E., Coggon, J. A., & Godard, M. (2018). In situ carbon mineralization in ultramafic rocks: Natural processes and possible engineered methods. Energy Procedia, 146, 92-102.
Kelemen, P. B., & Hirth, G. (2012). Reaction-driven cracking during retrograde metamorphism: Olivine hydration and carbonation. *Earth and Planetary Science Letters, 345*, 81-89.
Kelemen, P. B., & Matter, J. (2008). In situ carbonation of peridotite for CO2 storage. *Proceedings of the National Academy of Sciences,* https://doi.org/10.1073/pnas.0805794105.
Kuleci, H., Schmidt, C., Rybacki, E., Petrishcheva, E., & Abart, R. (2016). Hydration of periclase at 350°CC to 620°C and 200 MPa: experimental calibration of reaction rate. *Mineralogy and Petrology, 110*(1), 1-10.
Lafay, R. Montes-Hernandez, G., Renard, F. (2018) Experimental evidence of reaction-induced micro-cracking and vein patterning during serpentinization of olivine, *Minerals*, 8, 412; doi:10.3390/min8090412.
Lambart, S., Savage, H. M., Robinson, B. G., & Kelemen, P. B. (2018). Experimental Investigation of the Pressure of Crystallization of Ca (OH) 2: Implications for the Reactive Cracking Process. *Geochemistry, Geophysics, Geosystems*, 19(9), 3448-3458.
Lisabeth, H., Zhu, W., Kelemen, P., & Ilgen, A. (2017). Experimental evidence for chemo-mechanical coupling during carbon mineralization in ultramafic rocks. *Earth and Planetary Science Letters, 474*, 355-367.
Louis, L., Wong, T.-F., & Baud, P. (2007). Imaging strain localization by X-ray radiography and digital image correlation: Deformation bands in Rothbach sandstone. *Journal of Structural Geology, 29*(1), 129-140.
Macdonald, A., & Fyfe, W. (1985). Rate of serpentinization in seafloor environments. *Tectonophysics, 116*(1-2), 123-135.
Malvoisin, B., Brantut, N., & Kaczmarek, M.-A. (2017). Control of serpentinisation rate by reaction-induced cracking. *Earth and Planetary Science Letters, 476*, 143-152.
Malvoisin, B., Brunet, F., Carlut, J., Rouméjon, S., & Cannat, M. (2012). Serpentinization of oceanic peridotites: 2. Kinetics and processes of San Carlos olivine hydrothermal alteration. *Journal of Geophysical Research: Solid Earth, 117*(B4), https://doi.org/10.1029/2011JB008842.
McBeck, J., Kobchenko, M., Hall, S. A., Tudisco, E., Cordonnier, B., Meakin, P., Renard, F. (2018) Investigating the onset of strain localization within anisotropic shale using digital volume correlation of time-resolved X-ray microtomography images. *Journal of Geophysical Research: Solid Earth*, https://doi.org/10.1029/2018JB015676.
Narr, W. (1991). Fracture density in the deep subsurface: techniques with application to point Arguello oil field (1). *AAPG Bulletin, 75*(8), 1300-1323.
Noiriel, C., Renard, F., Doan, M.-L., & Gratier, J.-P. (2010). Intense fracturing and fracture sealing induced by mineral growth in porous rocks. *Chemical Geology, 269*(3-4), 197-209.
O'Hanley, D. S. (1992). Solution to the volume problem in serpentinization. *Geology, 20*(8), 705-708.
O'Hanley, D. S. (1996). *Serpentinites: records of tectonic and petrological history*: Oxford University Press, New York, 277 pp.
Peuble, S., Andreani, M., Godard, M., Gouze, P., Barou, F., Van de Moortele, B., Mainprice, D., Reynard, B. (2015). Carbonate mineralization in percolated olivine aggregates: Linking effects of crystallographic orientation and fluid flow. *American Mineralogist, 100*(2-3), 474-482.

Accepted Article

© 2019 American Geophysical Union. All rights reserved.

Plümper, O., Beinlich, A., Bach, W., Janots, E., & Austrheim, H. (2014). Garnets within geode-like serpentinite veins: Implications for element transport, hydrogen production and life-supporting environment formation. *Geochimica et Cosmochimica Acta*, 141, 454-471.

Plümper, O., Røyne, A., Magrasó, A., & Jamtveit, B. (2012). The interface-scale mechanism of reaction-induced fracturing during serpentinization. *Geology, 40*(12), 1103-1106.

Price, N. J. (2016). *Fault and joint development: in brittle and semi-brittle rock*: Elsevier.

Ougier-Simonin, A., & Zhu, W. (2013). Effects of pore fluid pressure on slip behaviors: An experimental study. *Geophysical Research Letters*, 40(11), 2619-2624.

Ougier-Simonin, A., & Zhu, W. (2015). Effect of pore pressure buildup on slowness of rupture propagation. *Journal of Geophysical Research: Solid Earth*, 120(12), 7966-7985.

Raleigh, C. B., & Paterson, M. (1965). Experimental deformation of serpentinite and its tectonic implications. *Journal of Geophysical Research, 70*(16), 3965-3985.

Renard, F., Cordonnier, B., Dysthe, D. K., Boller, E., Tafforeau, P., & Rack, A. (2016). A deformation rig for synchrotron microtomography studies of geomaterials under conditions down to 10 km depth in the Earth. *Journal of synchrotron radiation, 23*(4), 1030-1034.

Renard, F., McBeck, J., Cordonnier, B., Zheng, X., Kandula, N., Sanchez, et al. (2018) Dynamic in situ three-dimensional imaging and digital volume correlation reveal strain localization and fracture coalescence in sandstone, *Pure and Applied Geophysics*, http://dx.doi.org/10.1007/s00024-018-2003-x.

Rice, J. R. (1975). On the stability of dilatant hardening for saturated rock masses. *Journal of Geophysical Research, 80*(11), 1531-1536.

Rouméjon, S., Cannat, M., Agrinier, P., Godard, M., & Andreani, M. (2015). Serpentinization and fluid pathways in tectonically exhumed peridotites from the Southwest Indian Ridge (62–65 E). *Journal of Petrology, 56*(4), 703-734.

Rouméjon, S., & Cannat, M. (2014). Serpentinization of mantle‐derived peridotites at mid‐ocean ridges: Mesh texture development in the context of tectonic exhumation. *Geochemistry, Geophysics, Geosystems*, 15(6), 2354-2379.

Rudge, J. F., Kelemen, P. B., & Spiegelman, M. (2010). A simple model of reaction-induced cracking applied to serpentinization and carbonation of peridotite. *Earth and Planetary Science Letters, 291*(1-4), 215-227.

Scherer, G. W. (2004). Stress from crystallization of salt. *Cement and concrete research, 34*(9), 1613-1624.

Schmitt, D. R., & Zoback, M. D. (1992). Diminished pore pressure in low-porosity crystalline rock under tensional failure: Apparent strengthening by dilatancy. *Journal of Geophysical Research: Solid Earth*, 97(B1), 273-288.

Schlindwein, V., & Schmid, F. (2016). Mid-ocean-ridge seismicity reveals extreme types of ocean lithosphere. *Nature, 535*(7611), 276.

Scholz, C.H. (1968). The frequency–magnitude relation of microfracturing in rock and its relation to earthquakes. *Bull. Seismol. Soc. Am*., 58, 399–415.

Singh, C., Singh, S. (2015). Imaging b-value variation beneath the Pamir–Hindu Kush region. *Bull. Seismol. Soc. Am*. 105, 808–815. http://dx.doi.org/10.1785/0120140112.

Skarbek, R. M., Savage, H. M., Kelemen, P. B., & Yancopoulos, D. (2018). Competition between crystallization-induced expansion and creep compaction during gypsum formation, and implications for serpentinization. *Journal of Geophysical Research: Solid Earth*, 123(7), 5372-5393.


Accepted Article

© 2019 American Geophysical Union. All rights reserved.

Song, I., Suh, M., Woo, Y.-K., & Hao, T. (2004). Determination of the elastic modulus set of foliated rocks from ultrasonic velocity measurements. *Engineering Geology, 72*(3-4), 293-308.

Tudisco, E., Hall, S., Charalamp idou, E., Kardjilov, N., Hilger, A., & Sone, H. (2015). Full field measurements of strain localisation in sandstone by neutron tomography and 3D volumetric digital image corr elation. *Physics Procedia*, 69, 509–515. https://doi.org/10.1016/j.phpro.2015.07.072.

Tudisco, E., Andò, E., Cailletaud, R., & Hall, S. A. (2017). TomoWarp2: a local digital volume correlation code. *SoftwareX, 6*, 267-270.

Tutolo, B. M., Mildner, D. F., Gagnon, C. V., Saar, M. O., & Seyfried Jr, W. E. (2016). Nanoscale constraints on porosity generation and fluid flow during serpentinization. *Geology, 44*(2), 103-106.

Ulven, O., Jamtveit, B., & Malthe ‐ Sørenssen, A. (2014). Reaction ‐ driven fracturing of porous rock. *Journal of Geophysical Research: Solid Earth, 119*(10), 7473-7486.

Van Noort, R., Wolterbeek, T., Drury, M., Kandianis, M., & Spiers, C. (2017). The force of crystallization and fracture propagation during in-situ carbonation of peridotite. *Minerals*, 7(10), 190.

Vasseur, J., Wadsworth, F.B., Lavallée, Y., Bell, A.F., Main, I.G., Dingwell, D.B. (2015). Heterogeneity: the key to failure forecasting. *Sci. Rep*. 5, 13259. http://dx.doi.org/10.1038/srep13259.

Viggiani, G., Lenoir, N., Bésuelle, P., Di Michiel, M., Marello, S., Desrues, J., & Kretzschmer, M. (2004). X-ray microtomography for studying localized deformation in fine-grained geomaterials under triaxial compression. *Comptes rendus. Mécanique, 332*(10), 819-826.

Wiemer, S., Benoit, J.P. (1996). Mapping the b-value anomaly at 100km depth in the Alaska and New Zealand subduction zones. *Geophys. Res. Lett.*, 23, 1557–1560.

Xing, T., Zhu, W., Fusseis, F., & Harrison, L. (2018). Generating porosity during olivine carbonation via dissolution channels and expansion cracks. *Solid Earth, 9*(4), 879-896.

Zheng, X., Cordonnier, B., Zhu, W., Renard, F., & Jamtveit, B. (2018). Effects of confinement on reaction−induced fracturing during hydration of periclase. *Geochemistry, Geophysics, Geosystems*, 19(8), 2661-2672.

Zhu, W., Fusseis, F., Lisabeth, H., Xing, T., Xiao, X., De Andrade, V., & Karato, S. i. (2016). Experimental evidence of reaction ‐ induced fracturing during olivine carbonation. *Geophysical research letters, 43*(18), 9535-9543.


Accepted Article

© 2019 American Geophysical Union. All rights reserved.

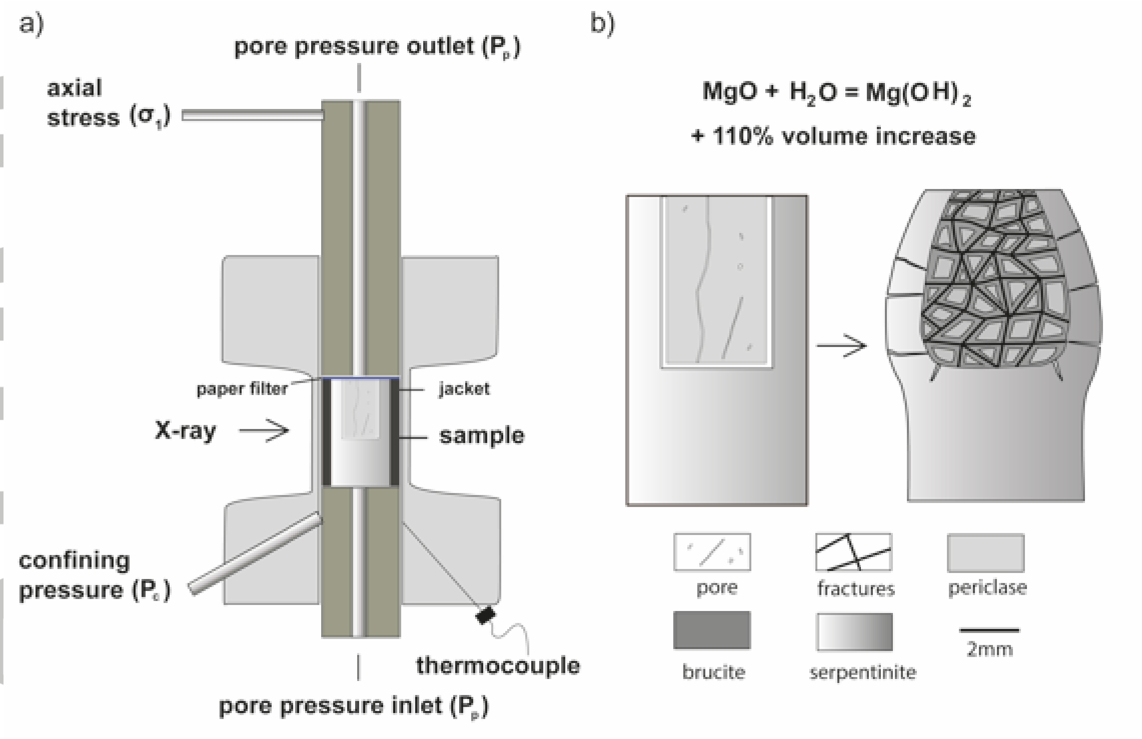


**Figure 1**. Experimental set-up and experimental conditions. a) Schematic diagram of the HADES triaxial deformation apparatus. b) Schematic diagram of the hydration reaction associated with the fracturing of both the periclase/brucite and the surrounding serpentinite cylinder.

Accepted Article

© 2019 American Geophysical Union. All rights reserved.

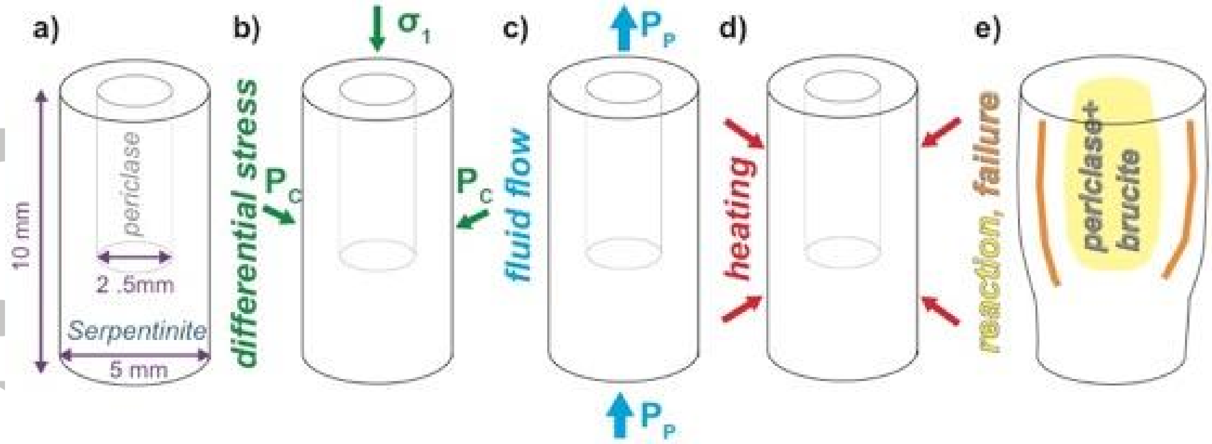


**Figure 2**. Experimental setup and procedure. a) A 2.5×5 mm periclase ceramics core was placed in a 5×10 mm serpentinite cylinder with a drill hole. b) The axial and confining pressures were imposed first. c) A fluid pressure was imposed with a small pressure gradient of 0.5 MPa between the pore fluid inlet and outlet of the sample to drive fluid flow. d) Then, the sample was heated at 2°C/min until the desired temperature (180°C or 190°C). e) Schematic representation of the expanded periclase/brucite sample after a period of volume increase due to the formation of brucite with associated fracturing of the serpentinite.

Accepted Article

© 2019 American Geophysical Union. All rights reserved.

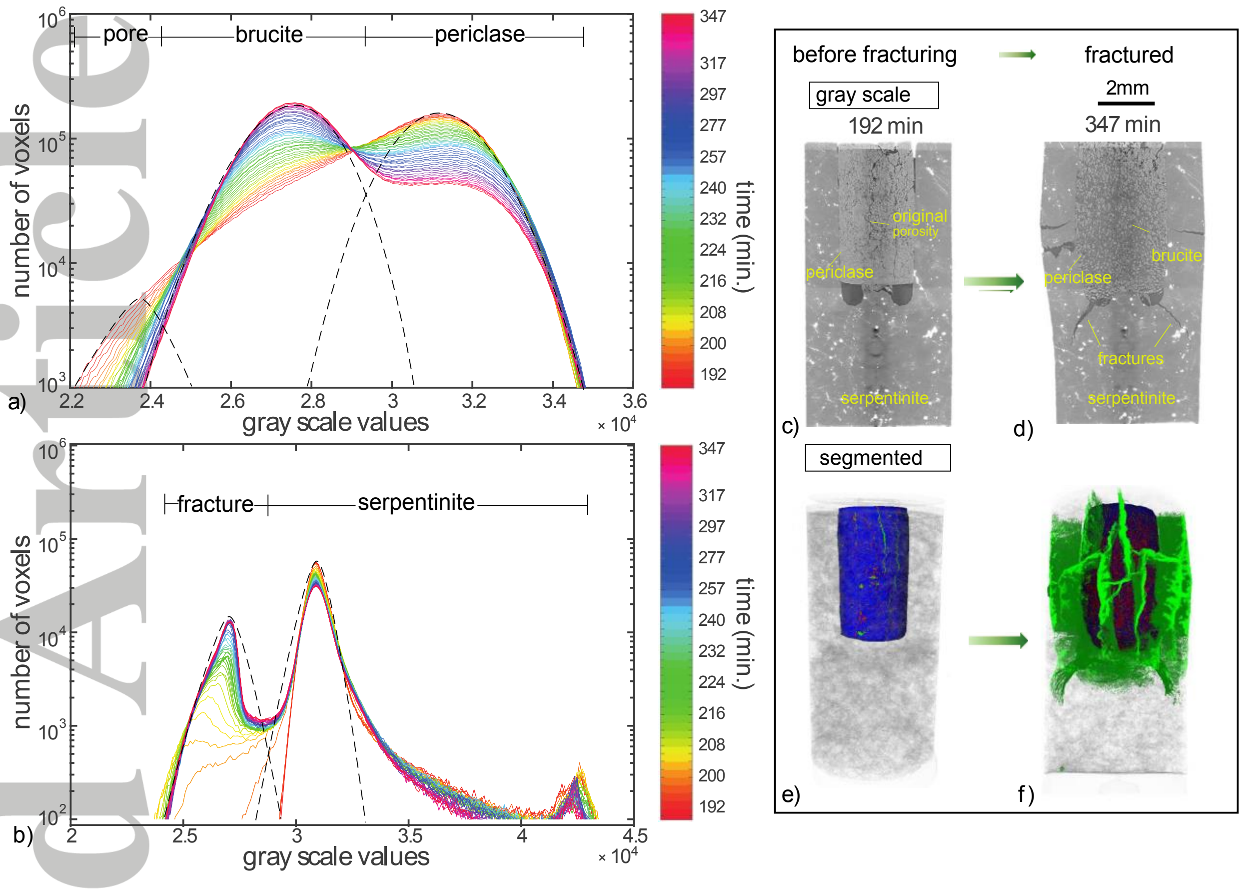


**Figure 3**. Segmentation of the different mineral phases and void space. a) Histograms of gray-scale values of the periclase cylinder in several microtomograms of sample Sp02 undergoing the periclase to brucite transformation. The histograms (solid curves) can be divided into three overlapping bell-shaped curves (dashed lines), which from small to large gray-scale values correspond to pore space, brucite and periclase. The periclase volume fraction decreased while the brucite fraction increased with time as the reaction progressed. b) Histograms of gray-scale values of the serpentinite in several microtomograms of sample Sp02 undergoing fracturing. Two bell-shaped curves correspond to the open fractures (lower gray-scale) and the serpentinite (higher gray-scale). c) Vertical gray-scale slice of a tomogram of sample Sp02 before reaction. d) Vertical gray-scale of a tomogram after reaction and fracturing. e) Segmented tomogram before the reaction in experiment Sp02. Blue indicates periclase, green indicates porosity and red indicates brucite. f) Segmented tomogram at the end of experiment. The 3D fracture network in the serpentinite is shown in green.

Accepted Article

© 2019 American Geophysical Union. All rights reserved.

Accepted Article

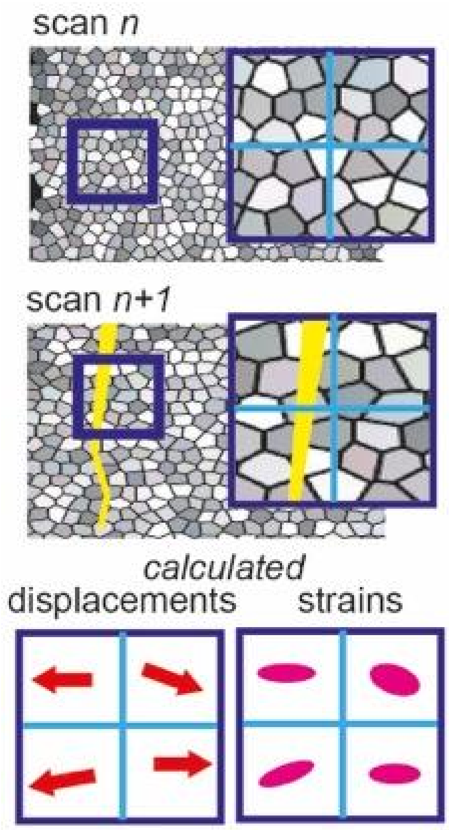


**Figure 4**. Schematic representation of digital volume correlation analysis. This technique estimates incremental displacement fields between tomogram pairs by matching patterns (gray polygons) across successive scans (i.e., scan *n* and scan *n*+1) within subvolumes (light blue squares). DVC analysis captures the inelastic and elastic contributions to deformation as fractures (yellow) propagate. The full incremental strain tensor (pink ellipses) can be calculated from the incremental displacement fields (red arrows).

© 2019 American Geophysical Union. All rights reserved.

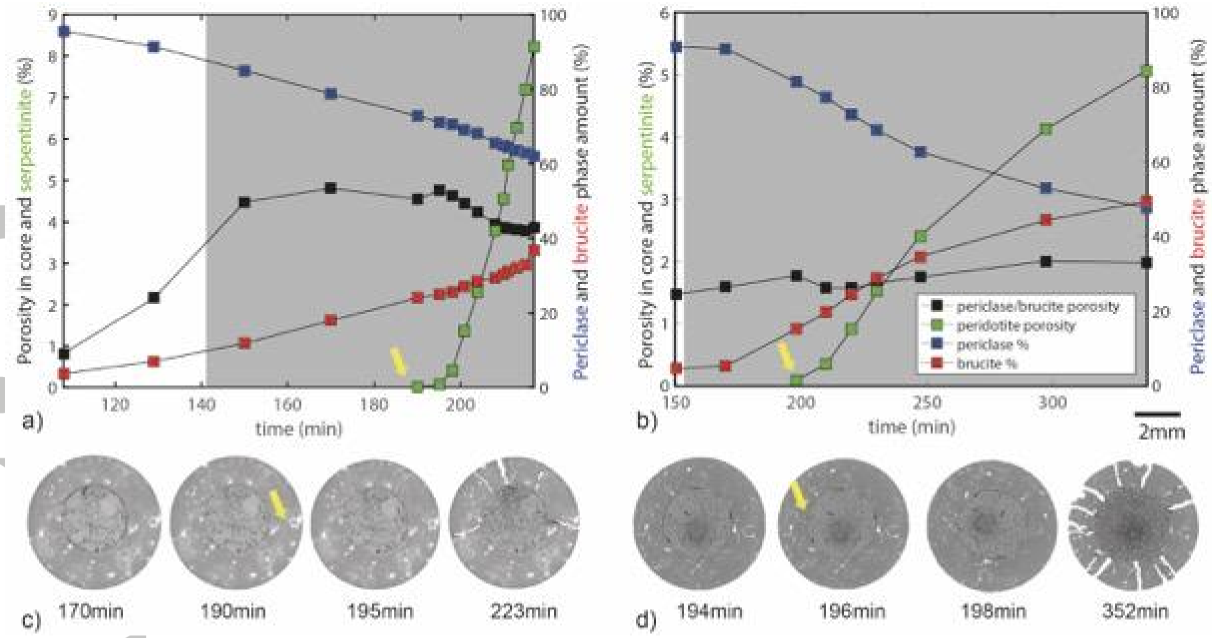


**Figure 5**. Evolution of the volume of periclase (blue), brucite (red), porosity within the periclase/brucite (black) and porosity with the serpentinite (green). a) Evolution of these phases in experiment Sp01. b) Evolution of the phases in experiment Sp02. Data are normalized by the maximum value of the corresponding parameter. Gray areas indicate the time windows where the digital volume correlation calculations were performed. Yellow arrows point to the appearance of the first fracture located for both samples at the inner serpentinite wall.

Accepted

© 2019 American Geophysical Union. All rights reserved.

Accepted Article

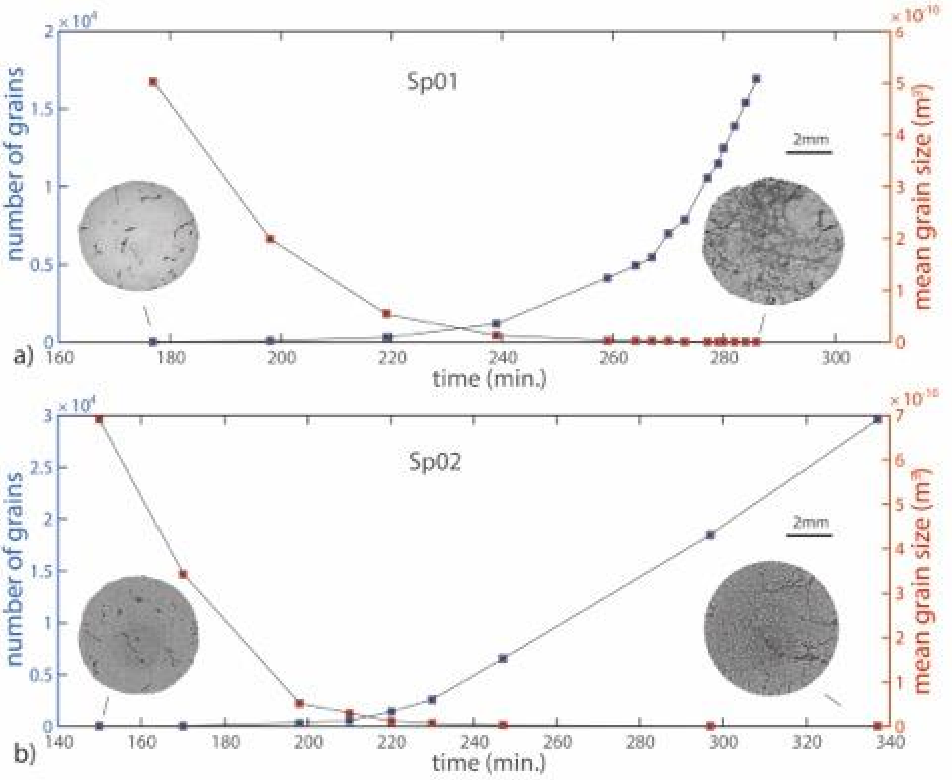


**Figure 6**. Grain size evolution in the periclase core in experiments Sp01 (a) and Sp02 (b). Blue curve represents the number of grains. Red curve displays the mean grain size at each time step.

© 2019 American Geophysical Union. All rights reserved.

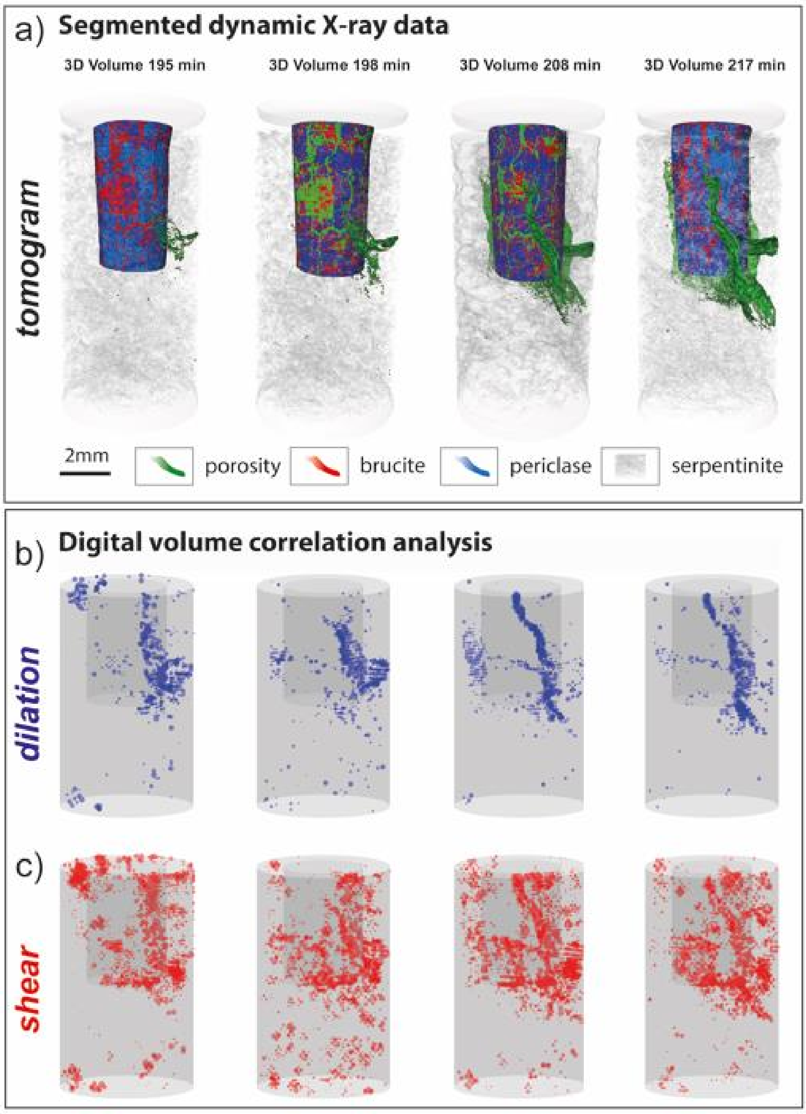


**Figure 7**. a) Three-dimensional views of the segmentation of sample Sp01. Green indicates fractures, blue indicates periclase, and red indicates brucite. Digital volume correlation estimates of incremental (b) dilatant (blue) and (c) shear strains (red) above the 90th percentile of the population. The sizes of the dots are proportional to the strain magnitude. Movie S3 shows the complete evolution of these strain components.

Accepted Article

© 2019 American Geophysical Union. All rights reserved.

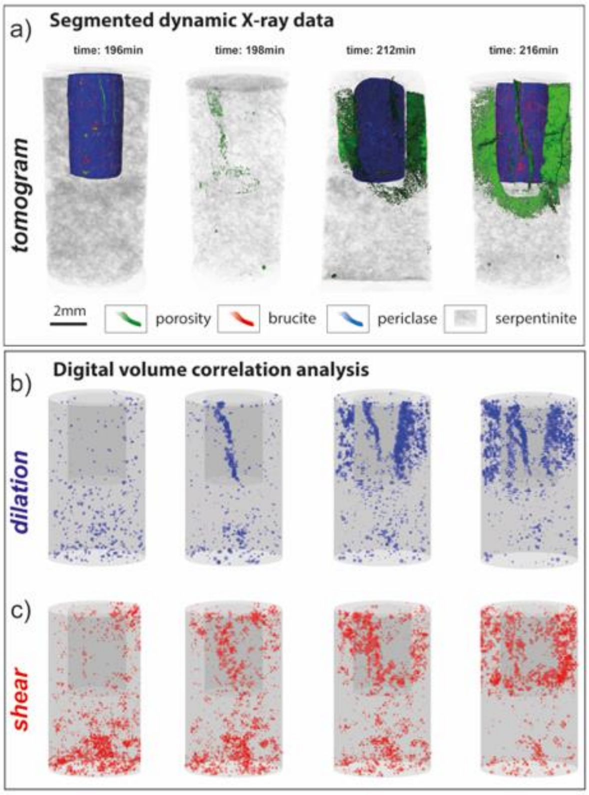


**Figure 8**. a) Three-dimensional view of the segmentation of sample Sp02. Note that at time 198 minutes, the periclase core was masked to show microfractures in the serpentinite more clearly. Green indicates fractures, red indicates brucite and blue indicates periclase. Digital volume correlation estimates of incremental (b) dilatant and (c) shear strains above the 90th percentile of the population. The sizes of the dots are proportional to the strain magnitude. Movie S4 shows the complete evolution of these strain components.

Accepted Article

© 2019 American Geophysical Union. All rights reserved.

Accepted Article

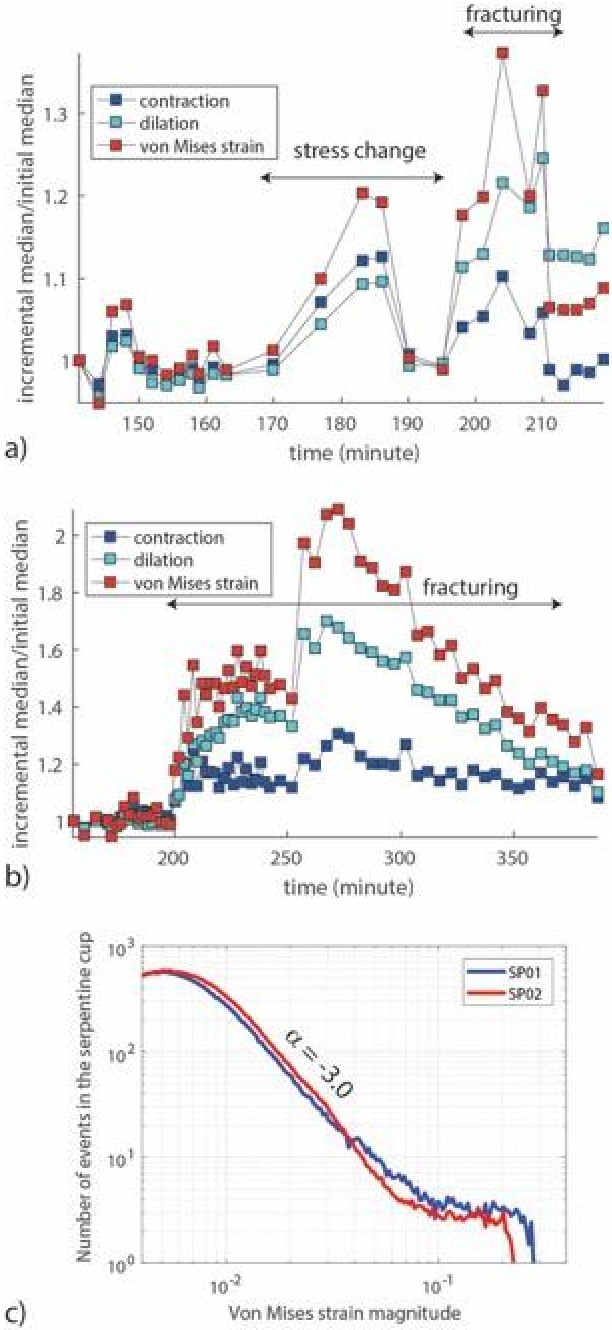


**Figure 9**. Incremental dilatant, contraction and von Mises strain in experiments Sp01 (a) and Sp02 (b). Fracturing produces changes in the magnitude of strains. c) Power law distribution of the magnitude of Von Mises shear strain events in the serpentinite. The slope $\alpha$ has a value of -3.0±0.2.

© 2019 American Geophysical Union. All rights reserved.

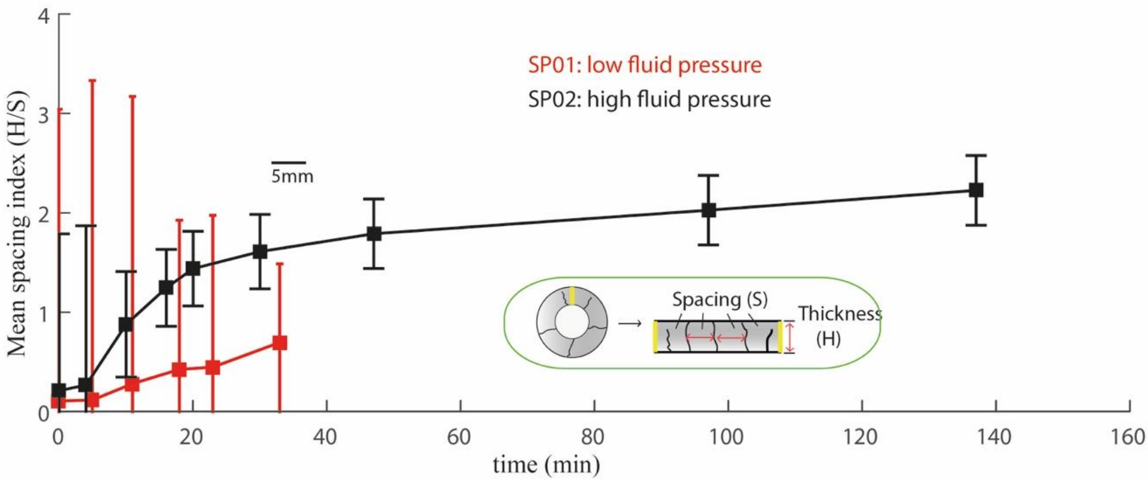


**Figure 10**. Evolution of mean fracture spacing index through time. The error bars show one standard deviation. Bottom inset: sketch of the definition of the spacing index, H/S. Here, the origin of time corresponds to 190 minutes for experiment Sp01 and 196 minutes for experiment Sp02 in the Figure 9. The space-time data of the fractures in the serpentinite for experiment Sp02 is shown in Supplementary Figure S2.

Accepted Article

© 2019 American Geophysical Union. All rights reserved.

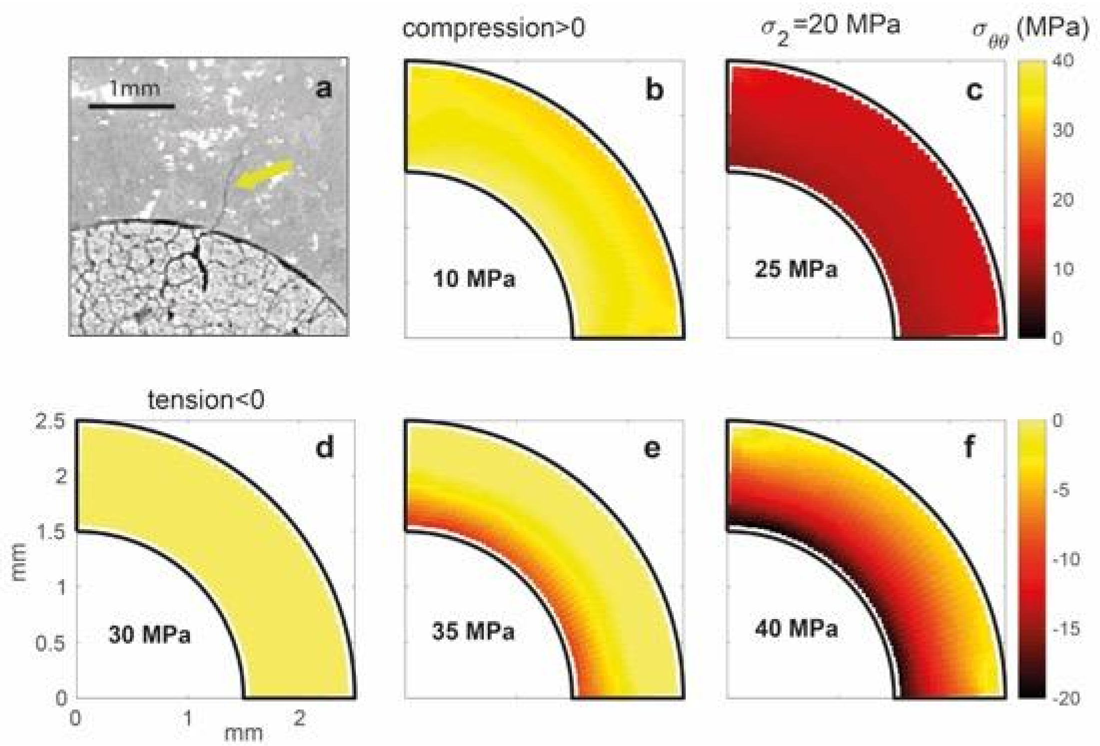


**Figure 11**. Investigation of the normal tangential stress distribution in the serpentinite. a) Horizontal slice of the tomogram when we observe the first fracture (yellow arrow) in the serpentinite wall of experiment Sp02. b-f) Normal tangential stress, $\sigma_{\theta\theta}$, distribution within horizontal slices of the serpentinite from 2D linear elastic mechanical models. Increasing normal stress on the inner wall of the serpentinite: b) 10 MPa, c) 25 MPa, d) 30 MPa, e) 35 MPa, and f) 40 MPa, with constant 20 MPa confining stress on the outside wall. When the normal stress exerted on the inner wall, $\sigma_i$ is equal or larger than 30 MPa, $\sigma_{\theta\theta}$, becomes tensile (negative). The largest magnitudes of $\sigma_{\theta\theta}$ develop near the inner wall, representing the contact between the brucite/periclase and serpentinite, consistent with the observed nucleation of the earliest fractures at the inner wall (a).

Accepted Article

© 2019 American Geophysical Union. All rights reserved.

Accepted Article

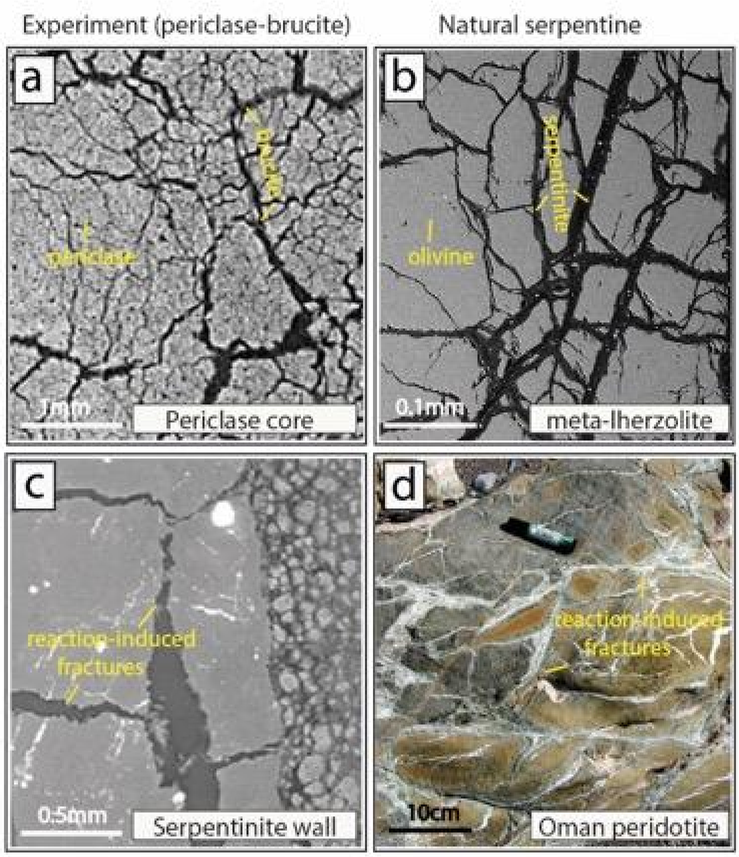


**Figure 12**. Comparison of experimental (a, c) and natural (b, d) observations. a) Tomography image showing hydration reaction in the periclase in our experiment. b) Mesh texture evolution during the replacement of olivine by serpentine in meta-dunite of a natural rock from Feragen, Norway. Image courtesy of Oliver Plümper (Plümper et al., 2014). c) Reaction-induced fracturing in the serpentinite in our experiment. d) Veins of serpentinites produced by reaction-induced fracturing in peridotites from Oman. Image courtesy of Stéphane Guillot.

© 2019 American Geophysical Union. All rights reserved.

**Table 1.** *Experimental conditions for all samples. Arrows represent changes of stress states in experiment Sp01 during reaction.*

| Test no. | $\sigma_1$ (MPa) | $P_c$ (MPa) | $P_p$ (MPa) | $\sigma_{eff}$ (MPa) | $\sigma_{diff.}$ (MPa) | T (℃) | t (min.) | $\Phi_0$ |
|---|---|---|---|---|---|---|---|---|
| Sp01 | 30→25→50 | 10→5 | 5 | 12→10→15 | 20→15→45 | 180 | 220 | 0.81 |
| Sp02 | 81 | 80 | 75 | 5 | 1 | 190 | 340 | 1.47 |

*Note.* $\sigma_1$ = axial stress, $\sigma_2 = \sigma_3 = P_c$ = confining pressure, $P_p$ = pore-fluid pressure, $\sigma_{eff} = (\sigma_1 + 2\sigma_2)/3 - P_p$ effective mean stress, $\sigma_{diff} = \sigma_1 - P_c$ differential stress, T = temperature, t = duration of experiment after temperature was stable and water was injected. $\Phi_0$ = initial porosity of periclase core.

Accepted Article

© 2019 American Geophysical Union. All rights reserved.